Sourcing limestone masonry for restoration of historic buildings, a spectroscopic pilot study

Laurence Hopkinson[1*](*corresponding author), Ken Rutt[2], Petra Kristova[2], Joan Blows[3], Callum Firth[1]

(1) School of the Environment and Technology,

University of Brighton

Cockcroft Building, Lewes Road, Brighton.BN2 4GJ.

United Kingdom.

Tel +44(0) 1273 642239, Fax: +44 (0) 642285, e.mail: l.hopkinson@brighton.ac.uk

Tel +44(0) 1273 642289, Fax: +44 (0) 642285, e.mail: c.firth@brighton.ac.uk

(2) School of Pharmacy and Biomolecular Sciences,

University of Brighton.

Huxley Building, Lewes Road, Brighton BN2 4GJ.

United Kingdom.

Tel: +44 (0)1273 642065, Fax: +44 (0)1273 642285, e.mail:

p.kristova@brighton.ac.uk

Tel: +44 (0)1273 642076, Fax: +44 (0)1273 642285, e.mail: k.j.rutt@brighton.ac.uk

(3) 51 Havelock Street

Canterbury, Kent CT1 1NP.

United Kingdom

e.mail: Tel: +44 (0)1227 472051, jfblows@btinternet.com

Key words mid-infrared, Raman, CIE *L*a*b**, limestone, masonry, provenance, environmental resource management

Abstract

This study presents a combined Fourier transform (FT) mid-infrared, laser Raman and Commission Internationale d'Eclairage (CIE) *L*a*b** system analysis of quarry-derived impure limestone and fallen masonry from a medieval listed building situated in the south east of England, to ascertain how spectroscopic information can be collectively employed to identify the most exacting possible replacement stone source. Data shows that subtle differences in [Al] and [Fe^{3+}] octahedral and tetrahedral site occupancy in glauconite group clays registered in the mid-infrared [3530cm^{-1}/3620cm^{-1}] absorption ratio exerts some influence on $L^*C_{ab}^*h_{ab}^*$ values. Increases in L^* and C_{ab} are associated with decreasing clay content. The overall weakness of correlations between infrared and visible range spectral attributes indicates multiple contributing sources to overall color. Evidence indicates that the degree of laser Raman induced background noise is related to the overall calcite content and that activators of fluorescence at 785nm excitation wave length may also contribute to rock color. The results are utilized to define closest matching quarry samples to the fallen masonry.

Introduction

Globally limestone has been worked for construction since antiquity. Consequently the assessment, management and allocation of the most suitable masonry stone for maintenance and repair of historic monuments and buildings has become important with respect to safeguarding cultural heritages (e.g., Cardell et al., 2007; Park and Shin 2009). The topic represents a scientific challenge partly because the geological

source originally exploited will show variability in physical and chemical properties and, in settings where construction spans the millennia buildings may be comprised of a variety of rock types divorced in terms of geographical source location and geological origin. Superimposed on these considerations is the fact that weathering of masonry may take many forms, be distinct from weathering of natural outcrops and, involve a diverse range of highly site specific biogenic and/or abiogenic natural and anthropogenic processes (e.g., Grossi et al., 2003; Cardell et al., 2007; Dewanckele et al., 2013). Hence replacement masonry needs not only be a good match in color and texture to the original, but also needs to be durable and weather in a fashion akin to the degraded masonry, therefore ideally sourced from the same geological strata (e.g., Blows et al., 2003). The upshot is an internationally recognised need to develop multidisciplinary approaches which augment important traditional approaches such as petrographic analysis, x-ray diffraction and subjective color assessment (e.g., Török and Přikryl 2010).

Comparatively recent approaches to limestone masonry characterisation utilizing color quantification by the Commission Internationale d'Eclairage (CIE) *L*a*b** system have been employed to good effect in the fields of limestone characterization, cleaning and architectural stone decay (e.g., Laboure et al., 2000; Viles et al., 2002; Thornbush and Viles 2004). While provenance studies of architectural marble by laser Raman have been undertaken independently to great effect (Jehlička et al., 2009), as have identification of clay-based pigments and sourcing carved stone by mid-infrared spectroscopy (Wisseman et al., 2012; Cheilakou 2014). In addition remote laser (lidar) induced fluorescence spectra has been applied to characterise the spectral attributes of historic monuments and

stones (e.g., Pantani et al., 2000). However, such approaches have been employed sparingly and in isolation. No studies to date have simultaneously employed (CIE) with mid-infrared and Raman data, although collectively these spectroscopic techniques will be sensitive to mineralogy, composition, texture, calcite crystallinity, color and the sources of color. Hence, such an approach may hold a key to advancing limestone provenance and restoration projects. This paper provides a pilot study examining spectroscopic attributes of quarry derived impure limestone (colloquially named Kentish ragstone) of southeast England and fallen masonry from a 15th century grade 1 listed building, donated by English Heritage (United Kingdom), to show how spectroscopic techniques can be harnessed to elucidate provenance of fallen historic masonry, contributing factors to visible range color attributes of rocks and to define the most suitable quarry-based strata for replacement stone selection.

Kentish Ragstone

The building stones of south east England that were worked and used in vernacular buildings were sourced from a variety of sedimentary formations which range in age (Lott and Cameron 2005). Of particular significance is the Lower Cretaceous succession which is divisible into a lower non-marine sequence (Wealden Group), and an upper interval of marine sediments comprising the Lower Greensand Group (Fig.1a) the Gault and, Upper Green sand formations (Lott and Cameron 2005). The Hythe Formation within the lower greensand group is the most important interval in the succession in terms of building stone resources. The formation shows considerable lithological variation vertically and laterally between limestones and sandstones (calcareous and non-calcareous) (Worrsam and Tatton-Brown 1993).

Locally the succession comprises alternations of hard, grey to blue grey colored bioclastic limestone (Ragstone) which are well lithified, widely range in detrital quartz, glauconite and authigenic microcrystalline quartz content (Fig.1b). The ragstones occur intercalated with poorly cemented sandstones frequently containing irregular laminae of argillaceous material (colloquial name Hassock). It is important to note that the term 'glauconite' encompasses a series of micas that includes di-octahedral interlayer deficient micas (Rieder et al., 1999), the end members of which are as yet undefined (Ospitali et al., 2008) and, are commonly important centres of green color pigmentation in stone masonry (Martinec et al., 2010).

Quarrying of ragstone has taken place since Roman times and at least 30 disused quarries have been identified. They are concentrated mainly in the Maidstone area (Figure 1b) where significant outcrops occur and where stone could be readily transported to London (Blows 2011). Prior to the Norman invasion (1066 A.D) ragstone together with glauconitic fine sandstone from the Upper Greensand in Surrey (Reigate stone), laminated fine sandstone/siltstone from the Thanet beds in Kent and flint constituted the principal building stones which underpinned the development of southeast England (Worrsam and Tatton-Brown 1993; Blows 2011). The intensive nature of the Norman building programme demanded importation of masonry from France. This bioclastic limestone 'Caen Stone' was widely used in the construction of cathedrals and castles (Howe 2001; Blows et al., 2003). With the reformation (16th Century) monastic destruction made much masonry stone available for reuse (Blows et al., 2011). Ragstone use diminished in the 17-19th century (Blows et al., 2003).

Recent high profile restoration projects have involved the importation of French limestones (Savonniérres and Lepine) (Blows et al., 2003). The net result today is that many historic buildings are comprised of an eclectic mix of construction materials with at least *ca* 800 listed buildings (e.g., the city walls at Canterbury and the Tower of London) sourced at least in part from Kentish ragstone (Blows 2011). The richness of the historical legacy of ragstone usage is catalogued in detail by Worrsam and Tatton-Brown (1993). Presently there is only one operational pit that extracts masonry grade ragstone (Hermitage quarry, Kent), although the need for local sourced materials for conservation is explicit and the resurgence in demand for building stone for conservation projects is recognised at Government and local levels, notably stimulating the development of the British Geological Survey (BGS) electronic data base BRITPITS which provides historical records and petrographic data to locate matching stone for conservationists (Hyslop et al., 2010).

Analytical methods and techniques

Eight freshly cut slabs of masonry grade Kentish ragstone sourced from Hermitage quarry and taken from separate stratigraphic horizons [samples R1-8], together with three slabs of French limestone: Caen stone [CAE], Lepine [LEP] and Savonniérres [SAV], plus specimens of Reigate stone [REI], high purity transparent calcite (Iceland spar) and a freshly cut section through fallen church masonry [CC] were analysed. Ragstone sample [R6] showed distinct 5cm thick pale colored layering and consequently was subdivided into two sub samples [R6A] and [R6B] respectively. Thin sections (7cm *x* 5cm) of each were examined by petrographic microscopy.

Raman analyses were conducted on freshly cut rock surfaces employing a Perkin Elmer IdentiCheck Raman spectrometer, fitted with a 785nm laser and continuous un-gated (dispersive) CCD detector. The measurements were performed using a fiber optic probe with a 100 μm spot size at a working distance of 7.5 mm. The samples were measured in the spectral range 2000 – 200cm^{-1}. Each spectrum was collected from 8 scans for 2 s using 70 mW laser power at room temperature and repeated between three and ten times on different areas of the same flat surface of a given rock to ascertain the intensity variation in the same stone versus the variation between different stones.

The same flat surfaces of the rocks were then measured in the visible region with a Perkin Elmer Lambda 35 spectrophotometer. Software enabled color evaluation was performed according to the Commission International d'Eclairage (CIECAT02) *L*a*b** system, employing the 2° standard observer, average north sky daylight. Freshly cut internal surfaces of the fallen church masonry (sample [CC]) were analysed as well as paler weathered external surfaces sample [CS]. All freshly cut samples were then lightly manually ground and subject to Fourier Transform mid-infrared analysis (FT-IR). The analyses were performed using a Perkin Elmer Spectrum 65. Data manipulation was performed using PeakFit (Jandel, Scientific Software). All spectral analyses were conducted at least three times on randomly selected samples to ensure representative spectral analyses. All data was collected at the University of Brighton (United Kingdom).

Petrography

It is established that ragstones are sufficiently variable in lithological character that it is difficult to select limited numbers of samples 'typical' of the many varieties that may be encountered in outcrops (Lott and Cameron 2005). The quarry ragstones are green grey to blue grey in color, with medium (0.25-1mm) to very coarse grained (1-2mm) sparite, occasionally cut by <1-2mm wide pale siliceous veins and calcite stylolites. The ragstones are largely devoid of macroscopic evidence for a bioclastic component. In thin section samples consist of 70-95% sparitic calcite, with accessory fine sand-sized rounded pellets of glauconite, detrital quartz, authigeneic chalcedony, micrite and opaques. The ragstones show similar proportions of calcite textural types and are classified as sparse (matrix supported) biosparites. Previous studies indicate that much bioclastic debris is ferroan spar-replaced, with identifiable fossil fragments restricted to relic non-ferroan grains. Recognisable fragments consist of bivalve debris, echinoid plates, foraminifera tests, ostracod valves, bryozoan and algal fragments (Lott and Cameron 2005). All are present in varying abundances in the ragstones examined in the present study. The fallen masonry sample, which is also a glauconite-bearing matrix supported biosparite contains a comparable fossil assemblage to all quarry ragstones and is comparable to four comparatively quartz and glauconite poor quarry ragstones. The salient petrographic characteristics of the samples are outlined in Table 1.

Mid-infrared [650-2000cm^{-1}] region

The mid-infrared spectra of calcite is well constrained (e.g., White 1974; Gunasekaran and Anbalagan 2007). In the 600-2000cm^{-1} region the Iceland spar powder shows the prominent v_3 [1407cm^{-1}] v_2 [873cm^{-1}] and v_4 [712cm^{-1}] vibrations of

the [CO_3^{2-}] anion in calcite (Fig. 2a). The sample also shows a low intensity band at 1085cm^{-1} coincident with the Raman active v_1 vibration of the [CO_3^{2-}] anion in calcite. Bands at [853cm^{-1}] and [1795cm^{-1}] have previously been assigned as calcite combination bands (Böttcher et al., 1997). The [LEP] and [SAV] spectra are indistinguishable from Iceland spar. Hence they are interpreted as pure (calcite) limestone. The spectrum of [CAE] shows the prominent bands associated with calcite and additional silicate-related bands in the [700-1250cm^{-1}] region (Fig. 2a). The most prominent feature at [*ca* 1090cm^{-1}] is attributed to SiO_4 antisymmetric stretching vibrations of α-quartz (e.g., Müller et al., 2012). The low intensity band at [1170cm^{-1}] and the couplet at [796cm^{-1}] and [778cm^{-1}] are also characteristic of α-quartz and are assigned to symmetrical stretching of [SiO_4] units (e.g., Cheilakou et al., 2014). In accordance with Beer's law that a linear relationship exists between absorbance and sample concentration (e.g., Petit 2006) the strength of absorption at [778cm^{-1}] plotted against [796cm^{-1}] can be used to gauge limestone α-quartz impurity content (Fig. 3).

Ragstone spectra show an additional pronounced peak at *ca* [1030cm^{-1}] with a shoulder at [*ca* 910cm^{-1}] consistent with [*v*Si-O-Al] and [δAl-OH] vibrations of sheet silicates (e.g., Farmer 1974, Cheilakou et al., 2014). Specifically the [*ca* 1030cm^{-1}] peak coincides with a strong absorption band reported for glauconite (Fig. 2b). The Reigate spectrum is distinguished from the Ragstone and Caen stone spectra by virtue of the absence of evidence for α-quartz, comparatively low absorption of the [CO_3^{2-}] internal modes, and very strong absorption at [*ca* 1030cm^{-1}]. The fallen church masonry shows comparable evidence for glauconite (Fig. 2c).The precise wavenumber of the strong *ca* [1030cm^{-1}] band varies as a function of the percentage

of expandable (montmorillonite) layers (Manghnani and Hower 1964). The peak fitted absorption wavenumber of the ragstones range from [995cm^{-1}] sample [R6B] to [1021cm^{-1}] for sample [R7]. Sample [CC] shows peak absorption at [1016cm^{-1}] suggesting that the quarry ragstone and fallen masonry contain expandable (montmorillonite) layers in the *ca* 10-30% region. In contrast sample Reigate shows an absorption peak at [1047cm^{-1}] suggesting expandable layers in excess of 40% (Manghnani and Hower 1964).

Figure 4 shows triangular-normalized peak absorption of the calcite v_3 band [1407cm^{-1}], the *ca* [1030cm^{-1}] sheet silicate band and, the [1090cm^{-1}] [Si-O-Si] α-quartz band for all samples subsequent to Iceland spar background subtraction at [1030cm^{-1}] and [1090cm^{-1}] respectively. The Ragstone samples define a field with respect to relative strength of normalized absorption at the three frequencies of interest which distinguishes them from all exotics. The fallen church masonry [CC] plots in the vicinity of comparatively calcite-rich ragstones.

Mid-infrared [2400-4000cm^{-1}] region

The samples Iceland spar, [SAV] and [LEP] show bands at *ca* [2506cm^{-1}] with shoulders at [2590cm^{-1}] and [2977cm^{-1}], together with bands at [2865cm^{-1}] and [2975cm^{-1}] which have previously been assigned to calcite overtones (Schenk et al., 1986). Ragstone samples, [CAE], [CC] and [REI] also show low intensity multi-component broad absorption band(s) in the *ca* [3200cm^{-1} - 3400cm^{-1}] region. For α-quartz the *ca* [3400cm^{-1}] band is interpreted to result from superposition of molecular water from fluid inclusions and hydrogen bonded surface group bands (Flörke et al.,

1982; Frondel 1982; Graetsch et al. 1987). Sheet silicates similarly yield broad band absorption in this region, including glauconite group clays for which maximum absorption is given at [3428cm^{-1}] (Moretto 2011). Hence the broad spectral feature in the *ca* [3200cm^{-1} - 3400cm^{-1}] registers total silicate hosted water.

Ragstones, [REI] and [CC] show numbers of variably resolved low intensity bands in the *ca* [3530-3640cm^{-1}] region (Fig. 5a-e) which coincide with structural [OH] stretching vibrations of minerals of the glauconite-celadonite-leucophyllite group (e.g., Slonimskaya et al., 1986). The samples show a variably resolved low intensity band at *ca* [3623cm^{-1}] assigned to [Al-OH] stretching vibration which is characteristic of muscovite (Farmer 1974; Slonimskaya et al., 1986; Moretto et al., 2011). The ragstones and [CC] also show a variably resolved band(s) at *ca* [3531cm^{-1}] closely coinciding with three closely spaced dioctahedral mica bands reported at [3528cm^{-1}], [3534cm^{-1}] and [3545cm^{-1}] respectively. The former is assigned to ferrous and ferric OH groups, the later to ferric iron OH groups (Slonimskaya et al., 1986). Because the [3528cm^{-1}] and [3534cm^{-1}] bands are at frequencies close to the sum of instrumental error the resultant band at [3531cm^{-1}] is frequently reported (Slonimskaya et al., 1986). The main variation in the composition of glauconite relates to iron and aluminium in octahedral position and interlayer potassium (Manghnani and Hower 1964) and, variability in the relative intensity of bands at [3620cm^{-1}] and [3531cm^{-1}] have been related in measure to variability in [Al] and [Fe^{3+}] octahedral and tetrahedral site occupancy (Slonimskaya et al., 1986). When expressed as the ratio [3530cm^{-1}/3620cm^{-1}] ragstone values range from 0.945 [R3] to 1.112 [R5]. Sample [CC] shows a ratio of 1.042. Sample [R2] provides the closest match to [CC] in terms of ferric iron and aluminium crystal-chemical make-up.

Laser Raman Analysis

The application of Raman spectroscopy to finger-print carbonates is well documented (e.g., White 1974; Edwards et al., 2005; Gunasekaran and Anbalagan 2007; Sun et al., 2014), as is the issue of excessive background noise associated commonly with laser induced fluorescence, which is frequently encountered when dealing with natural calcite crystals and which at its extreme makes it impossible to obtain valid Raman spectra (e.g., Aminzadeh 1997; Gaft et al., 1998). In addition sample morphology, defect structure, crystallinity and grain size/porosity variability can also generate excessive background scattering. Therefore an array of sample specific physical and chemical attributes may serve to degrade or obscure the Raman signal.

Due to the extreme background noise induced by the operating conditions employed in this study valid Raman spectra were not obtained from samples [LEP] and [SAV]. All remaining Raman spectra show low intensity peaks superimposed on a broad generally high sloping background (Fig. 6a), suggestive of noise originating primarily from fluorescence (e.g., Vitek et al., 2012). Photo-bleaching had no effect on improving Raman signal to background noise. Of the samples from which a Raman signal was attained the symmetrical stretching mode of the [CO_3^{2-}] anion at *ca* [1088cm^{-1}] and calcite-assigned lattice modes at [282 and 156cm^{-1}] were resolved. The low intensity v_3 and v_4 vibrations of calcite reported at [1436cm^{-1}] and [713cm^{-1}] respectively (Edwards et al., 2005) were either unresolved or barely resolved. Also resolved to variable extents in some samples were extremely low intensity bands in the *ca* [545, 445, and 380cm^{-1}] regions, broadly coincident with previously described

Raman active bands for glauconite group minerals (Ospitali et al., 2008) together with evidence for extremely low intensity bands in the vicinity of [465cm^{-1}] and [207cm^{-1}] consistent with α-quartz. The degree of background noise expressed as intensity units *(I)* per cm^{-1} [(*I* at 200cm^{-1} – *I* at 2000cm^{-1}) / 1800cm^{-1}] ranges from 108.15 *I* per cm^{-1} (sample [CAEN]) to 11.75 *I* per cm^{-1} (sample [R8]). The standard deviation derived from ten analyses of a single sample is ± 14.90. Fig. 6b shows sample *I* per cm^{-1} values minus the corresponding value for [CC]. It is evident that [CC] shows similar fluorescence background noise to the quarry ragstones.

Visible range Analysis

The CIE *L*a*b** color model is defined by *(a*)* which represents how red or green a color is (where negative values indicate green and positive indicates red); *b** indicates how blue or yellow a color is (where negative equals blue and positive indicates yellow) and the lightness of the color *(L*)* (where 0 = black, 100 = white). The precision of these units is typically *ca* ± 0.1 unit (e.g., Labouŕe et al., 2000). Any color is described by the lightness (*L**) chroma (C_{ab}*) and hue (h_{ab}*) where C_{ab}* = $\sqrt{(a^{*2} + b^{*2})}$ is the radial component and h_{ab}* = arc tan *b**/*a**. Fig. 7a shows the samples examined in this study plotted in cylindrical *L**, C_{ab}*, h_{ab}* space. It is evident that [CC] plots within the general field of color space defined by ragstones. It is also evident from the *L**, C_{ab}*, h_{ab}* data from cut internal surface of the fallen masonry [CC] relative to exterior surfaces of the masonry [CS] that chromatic weathering involved an increase in chroma and slight lightening while the hue remained relatively constant (Fig. 7a). It has previously been reported that ragstone color can

change as a function of glauconite oxidation during weathering (Lott and Cameron 2005).

Color is frequently expressed as a single metric $E* = \sqrt{((L* \times L*) + (a* \times a*) + (b* \times b*))}$ and can be employed to ascertain total color difference (ΔE^*) based on L^*,a^*,b^* color difference of samples relative to [CC], where $\Delta E^* = \sqrt{((L* - L*[CC])2 + (a* - a*[CC])2 + (b* - b*[CC])2)}$ indicates that [R7] shows closest approach to [CC] (Fig. 7b). Guidelines for tolerance of acceptable color difference in the context of replacement stone suitability in relation to the research documented here do not exist. However it is interesting to note that $\Delta E^* \approx 2.3$ is cited as constituting a just noticeable difference in digital image processes (Sharma 2003).

Interpretation

It is evident that the four closest visible range color matches to [CC] in L^*, C_{ab}^*, h_{ab}^* and ΔE^* space show the closest matching spectral attributes in the [600cm^{-1} to 2000cm^{-1}] mid-infrared region (Fig. 3), i.e. relatively calcite-rich ragstones, which also show a comparatively discreet range of values in $L^*C_{ab}^*$ h_{ab}^* space (Figure 6a). Of these in terms of the visible color in ΔE^* space and mineralogical make-up sample [R7] provides the closest match to the fallen masonry [CC]. In terms of petrography sample [R7] is slightly coarser grained, more authigenic silica-rich and bioclast-poor than [CC]. However all ragstones and sample [CC] show seemingly random surges in calcite crystal sizes and contain at least some authigenic silica. Hence petrographic disparities between [CC] and [R7] may well be encompassed in the natural variability inherent in any individual ragstone in relation to the dimensions of

an individual thin section employed. Furthermore the ‘closeness’ of the nearest match quarry rock type to [CC] must be seen in the context of the quarry representing the single present day source of masonry grade ragstone.

Specific causes for the colors exhibited by ragstone are not known in detail beyond the fact that common to all are varying but limited abundances of glauconite. For any given mineral the visual effect of color stems from some combination of intrinsic constituents, impurities, defects and specific structures. Physical formalisms of these parameters for specific minerals reside in crystal field theory, molecular orbital theory, band theory and physical optics (Nassau 1978). Complications arise from the fact that more than one type of color-causing agent can be present in a mineral (Nassau 1978). This complexity is greatly compounded when considering lithified aggregates of minerals, particularly given that glauconite constitutes a mineral group (Rieder et al., 1999). Hence the colors of ragstones are certain to be the sum product of multiple contributing factors.

Samples [LEP] [SAV] and [CAE] show the greatest lightness and chroma of all samples examined. The former two limestones contain only traces of impurities. The latter contains significant detrital quartz. All three are devoid of clays. Hence one visible range attribute of clay based impurity in limestones appears to be an overall lowering of lightness and saturation. In this respect it is interesting to note that [R1] shows the lowest chroma and lightness of any sample is glauconite-rich (Table 1). However, the silicate-rich ragstone sample [R3] shows a very similar infrared spectral profile to [R1] in the [600cm^{-1}-2000cm^{-1}] region and, by inference extensively similar proportions of clays, quartz and calcite (Figure 3). Yet [R3] shows the

greatest L^* of all ragstones, and is widely separated in L^*, C_{ab}^*, h_{ab}^* space from [R1] (Fig. 7a), Further, a very weak negative correlation exists (r = -0.57 at the 95% confidence level) between the [3530cm^{-1}/3620cm^{-1}] ratio and E^* (Table 2). Hence within the limits of resolution afforded by FT-IR to detect traces of clay-based absorption in the [OH] region, data suggests that the greater the site occupancy by iron relative to aluminium in glauconite the lower the L^* value and corresponding C_{ab}^*. Therefore FT-IR evidence suggests that chemistry of the glauconite group contributes to color as well as overall modal abundance of the mineral group. However the weakness of the correlation between E^* and [3530cm^{-1}/3620cm^{-1}] must also reflect the multiple nature of the parameters contributing to visible color. In this respect it is of note that sample [R2] shows the closest match to [CC] in terms of ferric iron and aluminium crystal-chemical make-up, yet [R7] provides the overall closest match to [CC] in terms of ΔE^*.

A positive correlation (r = 0.61 at the 95% confidence level) exists between the strength of absorption at [1404cm^{-1}] and the magnitude of Raman background noise and a corresponding weak negative correlation (r = $^{-}$0.57) between Raman background noise and the intensity of absorption at *ca* [1030cm^{-1}], suggesting an association between the abundance of calcite and Raman background noise (Table 1). Known fluorescence centres in calcite include Mn^{2+} and various trace elements (Aminzadeh 1997; Gaft et al., 1998), structural defects and, organic centres such as bitumen, kerogens and caratones (e.g., Wang et al., 1997; Urmos et al., 1991; Bozlee et al., 2005). Raman background noise can also vary with energy transfer within crystals, sensitization, reabsorption and quenching (Marfunin 1979). The calcite component of ragstones is biogenic in origin and has been subject to patchy

ferroan spar replacement (Lott and Cameron 2005). Hence the rocks are transition metal bearing and, at least a fraction of the accessory opaque material identified in thin section is likely organic in origin and unresolvable by FT-IR due to either low concentrations and or partial overlap of organic bands with calcite overtones.

Although the causative activators of fluorescence cannot be categorically resolved by petrography positive correlations (95% confidence level) between Raman background noise with E^* (r = 0.58) and C_{ab}^* (r=0.66) suggests that at least some of the fluorescence activator(s) may also possess visible range spectral attributes. However because the intensity of background is specific to the wavelength employed, the objective, the power, the focusing et cetera it seems unlikely that fluorescence background alone could not be used as a diagnostic tool, but instead a secondary additional element to reinforce an hypothesis.

Conclusions

Petrographic analysis suggests any one of four possible relatively silicate impurity-poor quarry-derived limestone horizons as most suitable close matches to the fallen historic masonry. From these L^*, C_{ab}^*, h_{ab}^* values in conjunction with absorption characteristics in the [600cm^{-1} to 2000cm^{-1}] mid-infrared region independently identify a single stratigraphic horizon [R7] within the quarry as the closest matching limestone to the fallen historic masonry. Hence integrating CIE $L^*a^*b^*$, mid-infrared and Raman analysis shows potential as tool for quarry resource management. It is conceivable that the advent of expanded spectroscopic data sets could facilitate development of quantified spectroscopic replacement stone criteria to augment

existing approaches to provenance studies and resource management. The questions then become what constitute acceptable differences between the various spectroscopic attributes that define each limestone and the historic masonry they are designed to replace.

Acknowledgements

Gallagher Group Company is thanked for access to limestone samples. English Heritage is likewise thanked for supply of fallen historic masonry. The University of Brighton is thanked for financial support. The reviewers and editor are thanked for their valuable input.

References

Aminzadeh A (1997) Fluorescence bands in the FT-Raman spectra of some calcium minerals. Spectrochim. Acta. A53: 693-697

Blows J.F., Carey P.J., Poole A.B (2003) Preliminary investigations into Caen Stone in the U.K; its use, weathering and comparison with repair stone. Build. Environ. 38: 1143-1149.

Blows J.F (2011) Strategic Stone Study, a building stone atlas of Kent. English Heritage.

Böttcher M.E., Gehlken P., Steele D.F (1997) Characterization of inorganic and biogenic magnesian calcites by Fourier Transform infrared spectroscopy. Solid State Ionics. 101-103: 1379-1385.

Bozlee B.J., Misra A.K., Sharma S.K., Ingram M (2005) Remote Raman and fluorescence studies of mineral samples. Spectrochim. Acta A61: 2342-2348.

Cardell C., Benavente D., Rodŕiguez-Gordillo J (2007) Weathering of limestone building material by mixed sulphate solutions. Characterization of stone microstructure, reaction products and decay forms. Materials Characterization. 59: 1371-1385.

Cheilakou E., Troullinos M., Koui M (2014) Identification of pigments on Byzantine wall paintings from Crete (14^{th} century AD) using non-invasive fiber optics diffuse reflectance spectroscopy. Journal Archaeological Sci. 41, 541-555.

Dewanckele J., Boone M.A., De Kock T., Boever W., Brabant L., Bonne M.N., Fronteau G., Dils J., Van Hoorebeke L., Jacobs P., Cnudde V (2013) Holistic approach to pre-existing flaws on the decay of two limestones. Sci. Total Environment. 447, 403-414.

Edwards, H.G.M.., Jorge Villar S.E., Jehlicka J., Munshi, T. (2005). FT-Raman spectroscopic study of calcium-rich and magnesium-rich carbonate minerals. Spectrochim. Acta. A61:2273–2280.

474 Farmer V.C. (1974) The layer silicates. In: V.C. Farmer, (ed). The infrared spectra of
475 minerals. Mineral. Soc. Monogr. 4:227–284.
476
477 Flörke OW., Köhler-Herbertz P., Langer K., Tönges I (1982) Water in microcrystalline
478 quartz of volcanic origin. Contrib. Mineral. Petrol. 80: 324-333.
479
480 Frondel C (1982) Structural hydroxyl in chalcedony (type B quartz). American
481 Mineral. 67: 1248-1257.
482
483 Gaft M., Reisfeld R., Panczer G., Blank PH., Boulon G (1998) Laser-induced time-
484 resolved luminescence of minerals. Spectrochim. Acta. A54: 2163–2175.
485
486 Graetsch H., Flörke O.W., Miehe G (1987) Structural defects in microcrystalline
487 silica. Phys. Chem. Miner. 14: 249-257.
488
489 Grossi C.M., Esbert R.M., Díaz-Pache F., Alonso F.J (2003) Soiling of building
490 stones in urban environments. Build. Environ. 38, 147-159.
491
492 Gunasekaran S., Anbalagan G (2007) Spectroscopic characterisation of natural
493 calcite minerals. Spectrochim. Acta. A68: 656-664.
494
495 Howe J.A (2001) The geology of building stones. Edward Arnold 1910-reprinted
496 edition. London: Donhead Publishing.
497

Hyslop E., McMillan A., Cameron D., Leslie A., Lott G (2010) Building stone databases in the UK: practical resource for conservation. Engineering Geol. 115: 143-148.

Jehlička J., Šťastná A., Přikryl R (2009) Raman spectral characterization of dispersed carbonaceous matter in decorative crystalline limestones. Spectrochim. Acta. A73: 404-409.

Labouŕe M., Bromlet P., Orial G., Wiedemann G., Simon-Boisson C (2000) Assessments of laser cleaning rate on limestone and sandstones. J. Cult. Heritage. S21-27.

Lott G., Cameron D (2005) The building stones of South East England : mineralogy and provenance. In: 10th Euroseminar on Microscopy Applied to Building Materials, Paisley, Scotland, 21st - 25th June 2005.

Manghnani M.H., Hower J (1964) Glauconites: cation exchange capacities and infrared spectra. Part II. Infrared absorption characteristics of glauconites. Amer. Miner. 49:1631-1642.

Marfunin A.S (1979) Spectroscopy, luminescence, and radiation centers in minerals. Springer-Verlag, Berlin, Heidelberg, New York.

521 Moretto L.M,, Orsega E.F, Mazzocchin G.A, (2011) Spectroscopic methods for the
522 analysis of celadonite and glauconite in Roman green wall paintings J. Cult. Heritage
523 12: 384–391.
524
525 Martinec P.M., Vavro M., Scucka J., Maslan M (2010) Properties and durability
526 assessment of glauconitic sandstone: a case study on Zamel sandstone from
527 Bohemian Cretaceous basin (Czech republic. Engineering Geol. 115:175-181.
528
529 Müller C.M., Molinelli A., Karlowatz M., Aleksandrov A., Orlando T., Mizaikoff B
530 (2012) Infrared attenuated total reflectance spectroscopy of quartz and silica micro-
531 and nanoparticulate films. J. Phys. Chem. C116: 37-43.
532
533 Nassau K (1978) The origins of color in minerals. Amer. Miner. 63: 219-229.
534
535 Ospitali F., Bersani D., Di Lonardo G., Lottici P.P (2008) 'Green earths': vibrational
536 and elemental characterization of glauconites, celadonites and historical pigments. J.
537 Raman Spec. 39:1066-1073.
538
539 Pantani L., Ballerini G., Cecchi G., Edner H., Lognoli D., Johansson T., Raimondi V.,
540 Svanberg S., Tiano P., Tomaselli L., Weibring P (2000) Experiments on stony
541 monument monitoring by laser-induced fluorescence. J. Cult. Heritage 1:345-348.
542
543 Park H.D., Shin G.H (2009) Geotechnical and geological properties of Mokattam
544 limestones: Implications for conservation strategies for ancient Egyptian stone
545 monuments. Engineering Geol. 104:190-199.

Petit S (2006) Fourier transform infrared spectroscopy. In Bergaya F, Theng B.K.G, Lagalay G (eds) Handbook of clay science, vol. 1. Chapt.12: 909-918. Elseveir Ltd.

Radley J.D., Allen P (2012) The non-marine Lower Cretaceous Wealden strata of southern England. Proc. Geol. Assoc. 123: 245-318.

Rieder M., Cavazzini G., D'yakonov Yu.S., Frank-Kamenetskii V.A., Gottardi G., Guggenheim S., Koval P.V., Müller G., Neiva A.M.R., Radoslovich E.W., Robert J.L., Sassi F.P., Takeda H., Weiss Z., Wones D.R (1999) Nomenclature of the micas. Miner. Mag. 63:267-279.

Schenk H.J., Witte E.G., Müller P.J., Schwocha K (1986) Infrared estimates of aliphatic kerogen carbon in sedimentary rocks. Organic Geochem. 10:1099-1104.

Sharma, G (2003). Digital Color Imaging Handbook (1.7.2 ed.). CRC Press.

Slonimskaya M.V., Besson G., Dainyak L.G., Tchoubar C., Drits V.A (1986) Interpretation of the IR spectra of celadonites and glauconites in the region of OH-stretching frequencies. Clay Miner. 21:377-388.

Sun J., Wu Z., Cheng H., Zhang Z., Frost R.L (2014) A Raman spectroscopic comparision of calcite and dolomite. Spectrochim. Acta. A117:158-62.

570 Thornbush M., Viles H (2004) Integrated digital photography and image processing
571 for quantification of coloration on soiled limestone surfaces in Oxford, England. J.
572 Cult. Heritage. 5:285-290.
573
574 Török Á., Přikryl R (2010) Current methods and future trends in testing, durability
575 analyses and provenance studies of natural stones used in historic monuments.
576 Engineering Geol. 115:139-142.
577
578 Urmos J., Sharma S.K., Mackenzie F.T (1991) Characterisation of some biogenic
579 carbonates with Raman spectroscopy. Amer. Miner. 76: 641-646.
580
581 Vitek P., Ali E.M.A., Edwards H.G.M., Jehlička J., Cox R., Page K (2012) Evaluation
582 of portable Raman spectrometer with 1064nm excitation for geological and forensic
583 applications. Spectrochim. Acta. A86:320-327.
584
585 Viles H.A Taylor M.P, Yates T.J.S Massey S.W (2002) Soiling and decay of N.M.E.P
586 limestone tablets. Sci. Total Environ. 38, 147-159.
587
588 White, W. B. (1974). The carbonate minerals. In V. C., Farmer, ed. The infrared
589 spectra of minerals. Mineral. Soc. Monogr. 4:227–284.
590
591 Wisseman S.U., Hughes R.R., Emerson T.E., Farnsworth K.B (2012) Refining the
592 identification of native American pipestone quarries in the mid-continental United
593 States. J. Archaeological Sci. 39:2496-2505.
594

595 Worssam B.C., Tatton-Brown T (1993) Kentish Rag and other Kent building stones.
596 Archaeologia Cantiana. vol. CXll. 93-125.

597

598 **Captions**

599

600 **Table 1** Petrographic summary of samples. Modal abundances are based on semi-
601 quantitative visual assessment.

602

603 **Table 2** The correlation coefficient and significance (bracketed) for the various
604 measured spectral attributes. Correlation coefficients range from -1 through to +1. 0.
605 In general 0.05 or less is considered to be significant in environmental research (e.g.
606 5% of cases are wrong and 95% are right). The values marked in bold are significant
607 at the 95% confidence level.

608

609 **Figure 1 (a)** Simplified geological map of Kent adapted from Radley and Allen
610 (2012). **(b)** Diagrammatic vertical section through showing the west to east variation
611 in the lithological character of the Hythe beds between Sevenoaks and Ashford
612 (adapted from Worssam and Tatton-Brown 1993). The location of Hermitage quarry
613 is marked with a star.

614

615 **Figure 2 (a)** Mid-infrared spectra in the [600-2000cm^{-1}] region of interest, showing
616 **(a)** Pure calcite (solid line) and Caen stone (dashed line). **(b)** Reigate stone and
617 quarry ragstones. **(c)** Fallen church masonry.

618

619 **Figure 3** Strength of absorption at [796cm^{-1}] versus [778cm^{-1}] see text for details.

Figure 4 Triangular-normalized peak absorption of the calcite v_3 band [1407cm^{-1}], the *ca* [1030cm^{-1}] sheet silicate band and, the [1090cm^{-1}] (Si-O-Si) α-quartz band.

Figure 5 (a-e) FT-IR spectra of samples in the 2400cm^{-1} to 4000cm^{-1} region of interest. Sample identification is presented in a box next to each spectrum. See text for details. **(f)** Bar chart showing the [3530cm^{-1}/3620cm^{-1}] absorption intensity ratio of quarry samples minus the corresponding ratio for sample [CC].

Figure 6 (a) Examples of Raman spectra of limestones and Iceland spar. All spectra were acquired employing identical operating conditions **(b)** Bar chart showing the subtracted difference in intensity units per cm^{-1} relative to sample [CC].

Figure 7 (a) Ragstones and samples [CC], [CAE], [SAV],[LEP] and [REI] plotted in cylindrical $L^*C_{ab}^*h_{ab}^*$ space. The dashed circular line denotes the four closest ragstone matches to the fallen church masonry [CC]. The arrow denotes the path of chromatic weathering of the fallen church masonry from freshly cut internal surfaces sample [CC] to weathered exterior surfaces [CS]. **(b)** Bar chart showing the ΔE^* values of limestone samples relative to sample [CC].

Sample	Classification	Sparite	Bioclastic debris	Micrite	Detrital quartz	glauconite	Authigenic SiO_2	Opaque material	Others (e.g., illite, lithic fragments)	Summary description
R1	Biosparite	52	17	2	16	7	2	3	≤1	Coarse (0.5-1mm) sparite matrix, locally anastomosing <1mm wide very fine grained (ca 100μm) sparite veins and stylolites. Sparse very fine sand-sized sub-rounded quartz and glauconite locally defining laminations. Foliated bivalve shell fragments and disaggregated echinoderms common. Sparse traces of ostrocods, micritic walled foraminifera, bryozoans and nodular micritic algae present.
R2	Biosparite	58	27	3	5	3	1	2	≤1	Coarse (0.5-1mm) sparite matrix, randomly orientated elongate to sub rounded coarse sand-sized lithic fragments of glauconite-cemented silt-sized quartz grains, plus finer grained sub-rounded crystals of quartz and glauconite. Trace chalcedony infill. Bivalve shell fragments with foliated structures and disaggregated echinoderms common, Fragmented bryozoans, micritic walled foraminifera, articulated and disarticulated ostracods and sparse nodular micritic algae present.
R3	Biosparite	53	23	4	3	3	9	2	3	Medium grained (0.25-0.5mm) sparite matrix. Light pale blue grey 2cm-wide domains defined by chalcedony matrix with subordinate sparite. Cross-cut by styolites and glauconite-lined fractures flanked symmetrically by *ca* 2mm wide domains of very fine grained sparite. Foliated bivalve shell fragments and disaggregated echinoderms common, rich in micritic-walled foramanifera, ostracods plus fine sand sized micritic algae nodules. Transverse sections of bryozoans identified.
R4	Biosparite	56	17	9	6	7	2	2	1	Coarse (1-3mm) sparite maxtrix, medium to fine sand sized rounded particles of glauconite and detrital quartz, locally defining laminations. Trace illite present. nodular micritic algae. Foliated bivalve shell fragments, disaggregated echinoderms and micritic wall-lined formanifera and bryozoans present with rare ostracods.
R5	Biosparite	63	16	3	10	1	3	3	≤1	Medium grained (0.25-0.5mm) sparite cement, with dispersed medium to fine grained detrital crystals of quartz and glauconite. Foliated bivalve shell fragments and disaggregated echinoderms common, micritic wall-lined foraminifera, bryozoans, ostracods and algal micritic nodules identified.
R6A/B	Biosparite	72	15	2	3	4	1	2	≤1	Domains of very coarse grained sparite (1-3mm) hosting 3-5 cm wide discontinuous pale buff-grey coloured irregular-shaped enclaves devoid of bioclasts, composed of fine grained (0.25-0.5mm) sparite (R6A). The remainder of the sample (R6B) shows foliated bivalve shell fragments, disaggregated echinoderms, micritic wall-lined formanifera rare ostracods, algal nodules and evidence of bryozoans (R6B). Enclaves and host rock contain fine sand-sized detrital quartz and limited glauconite.
R7	Biosparite	52	18	7	6	5	8	3	≤1	Coarse grained (1-3mm) sparite, pale centimetre wide band rich in chalcedony. Sub-rounded detrital quartz and glauconite (medium to fine sand sized) arranged in sparite matrix supported laminations. Disaggregated echinoderms, nodular micritic algae (<1.5mm). Foliated bivalve shell fragments disaggregated echinoderms and micritic wall-lined foraminiferal tests common. Disarticulated ostracods, rare. Transverse sections of bryozoans identified. Sparse traces of brown coloured algal nodules range in size up to 1.5mm.
R8	Biosparite	64	17	3	6	3	4	2	≤1	Uniform very coarse (1-3mm) sparite, medium to fine grained sub-rounded detrital quartz and glauconite. Foliated bivalve shell fragments and disaggregated echinoderms common, micritic wall-lined foraminifera, ostracods, nodular micritic algae and fragmented bryozoan identified.
[CC]	Biosparite	60	22	8	3	2	1	3	≤1	Medium (0.25-0.5mm) to coarse grained (0.5-1mm) sparite matrix. Sparse fine sand sized clasts of detrital quartz and glauconite. Irregular ca 0.3mm wide *ca* 10mm long irregular calcite stylolites and chalcedony seams. Foliated bivalve and echinoderm shell fragments common, micritic-lined formaninifera tests present together with scare disarticulated and articulated ostracods. Fragmented bryozoans identified.
[REI]	Sandstone	12	5	5	2	58	5	2	11	Poorly lithified, friable and porous. Glauconite commonly occurring as rounded grains or as moulds of spicule chambers and foraminifera tests (Davies 1916). Note that the proportion of glauconite to Siliceous sponge spicules in Reigate stone can vary considerably and a detrital quartz component is commonly sparse or absent (Lott and Cameron 2005).
[CAE]	oobiosparite	37	15	30	12	0	0	5	≤1	Grain size <250μm. Matrix supported. Micritic wall-lined foraminifera tests and undifferentiated bioclastic debris.
[SAV]	oosparite	65	5	18	7	0	0	3	≤1	Grain supported. Ooids <2.5mm, matrix <125μm grain sizes.
[LEP]	oomicrite	22	4	66	3	0	0	5	≤1	Ooids <250μm, matrix supported (grain size <60μm).

639

	1034cm^{-1}	**1090cm^{-1}**	**1404cm^{-1}**	**3530cm^{-1}/3620cm^{-1}**	**Raman int. per cm^{-1}**	***C_{ab}****	***H_{ab}****
1090cm^{-1}	0.582**(0.029)**						
1404cm^{-1}	-0.876 **(0.000)**	-0.902 **(0.000)**					
3620cm^{-1}/3530cm^{-1}	0.217 (0.457)	-0.135 (0.645)	-0.035 (.906)				
Raman int. per cm^{-1}	-0.568 **(0.034)**	-0.524 (0.055)	0.612 **(0.020)**	-0.203 (0.486)			
C_{ab}*	-0.506 (0.065)	-0.168 (0.566)	0.368 (0.196)	-0.380 (0.180)	0.662 **(0.010)**		
H_{ab}*	0.421 (0.134)	0.122 (0.677)	-0.296 (0.305)	0.033 (0.910)	-0.378 (0.183)	-0.573 (0.032)	
E*	-0.451 (0.105)	0.022 (0.942)	0.226 (0.436)	-0.574 **(0.032)**	0.576 **(0.031)**	0.766 **(0.001)**	-0.435 (0.120)

Table 2

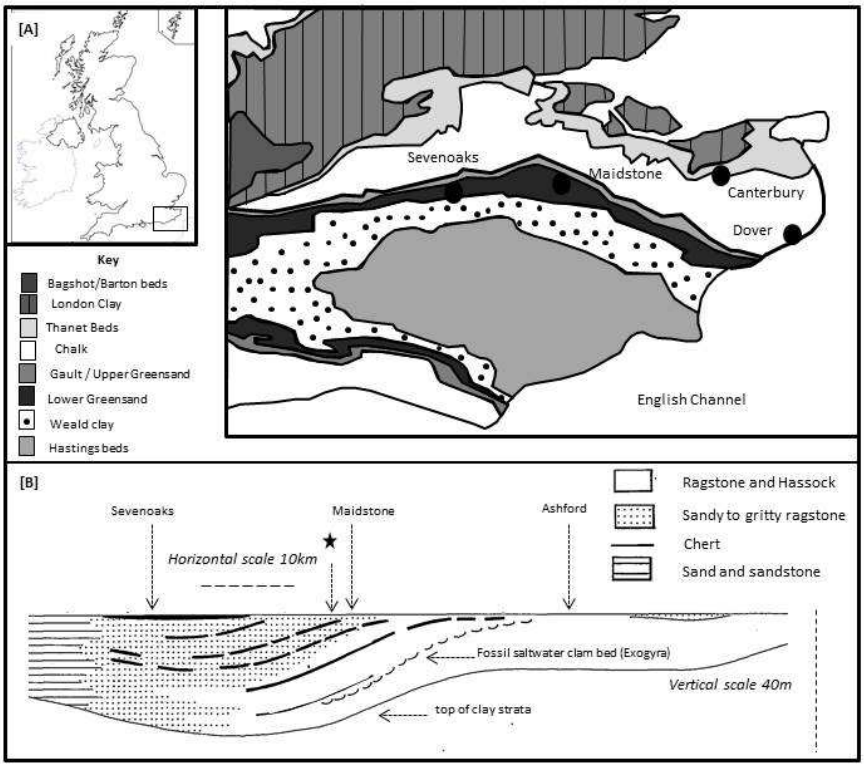

643

644 Figure 1

645

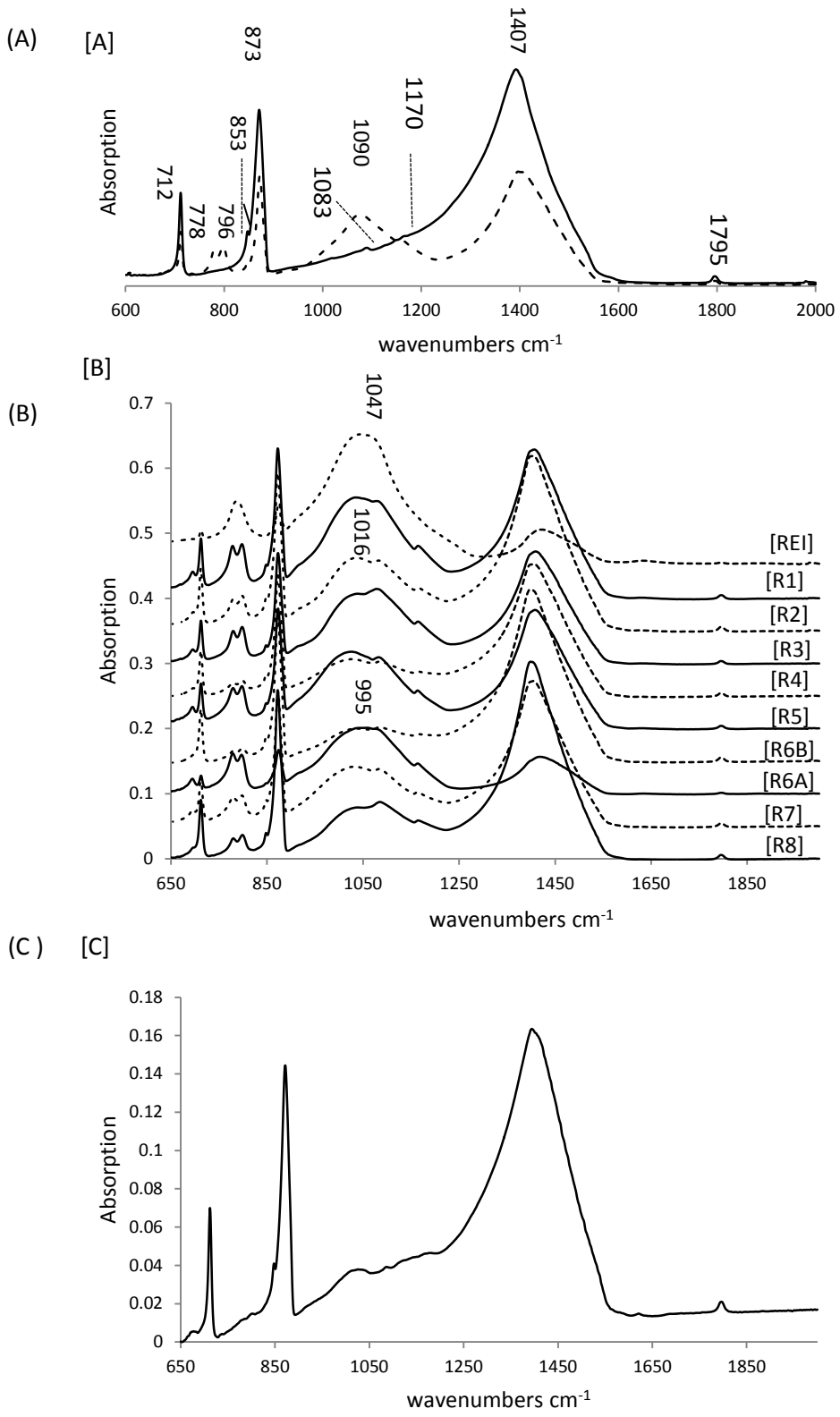
(A)
[A]
873
1407
1170
853
1090
1083
712
778
796
1795
Absorption
600
800
1000
1200
1400
1600
1800
2000
wavenumbers cm-1
[B]
(B)
1047
1016
995
[REI]
[R1]
[R2]
[R3]
[R4]
[R5]
[R6B]
[R6A]
[R7]
[R8]
Absorption
0.7
0.6
0.5
0.4
0.3
0.2
0.1
0
650
850
1050
1250
1450
1650
1850
wavenumbers cm-1
(C)
[C]
Absorption
0.18
0.16
0.14
0.12
0.1
0.08
0.06
0.04
0.02
0
650
850
1050
1250
1450
1650
1850
wavenumbers cm-1

646 Figure 2

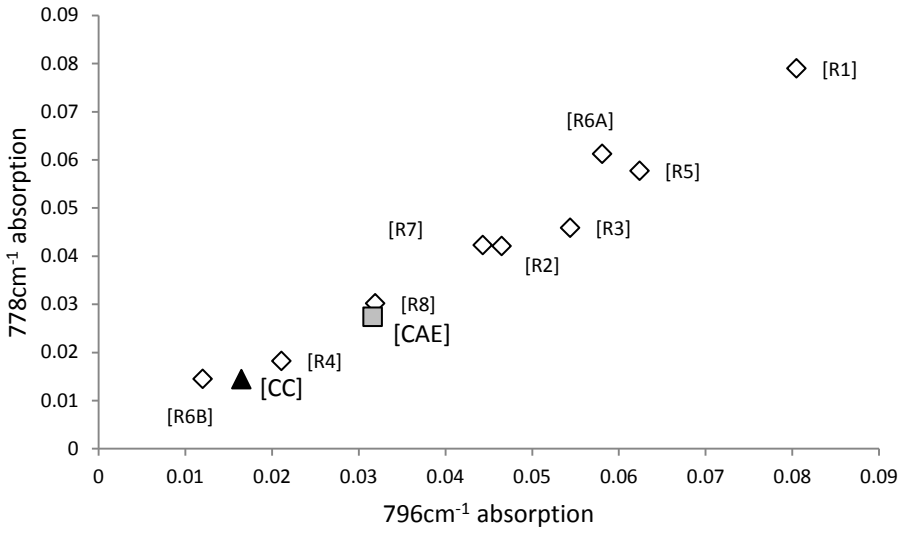

647

648 Figure 3

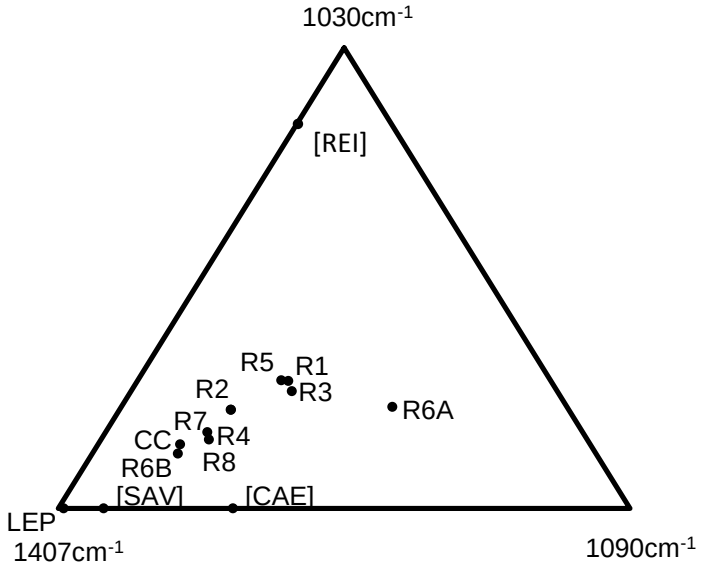

649

650 Figure 4

651

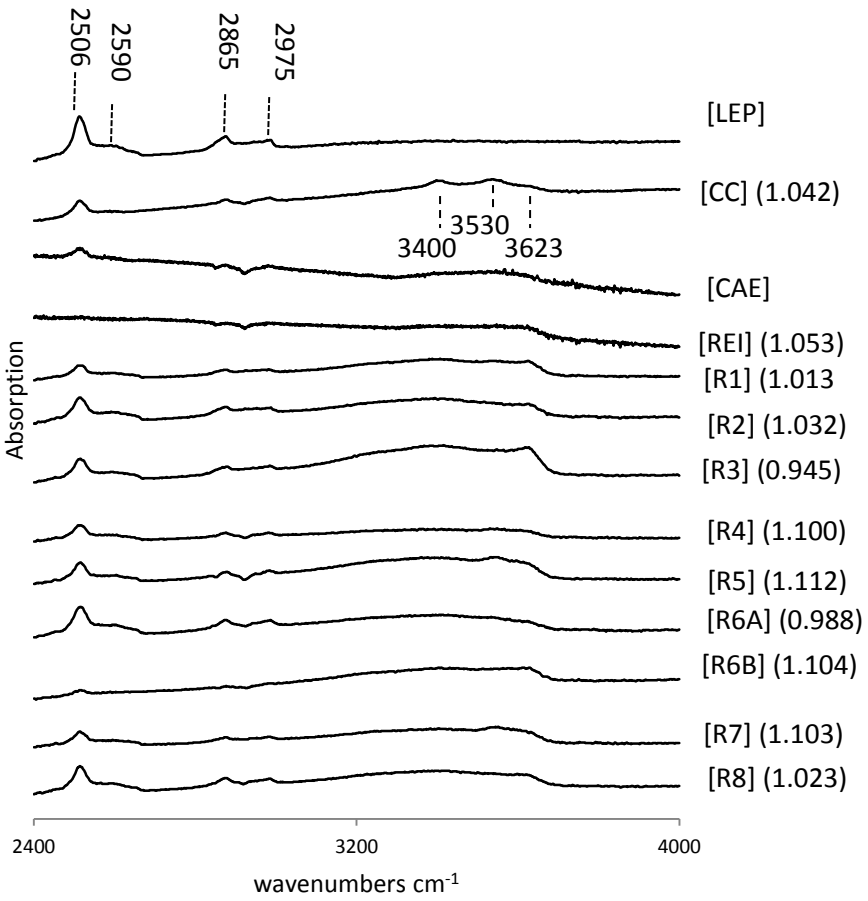

652

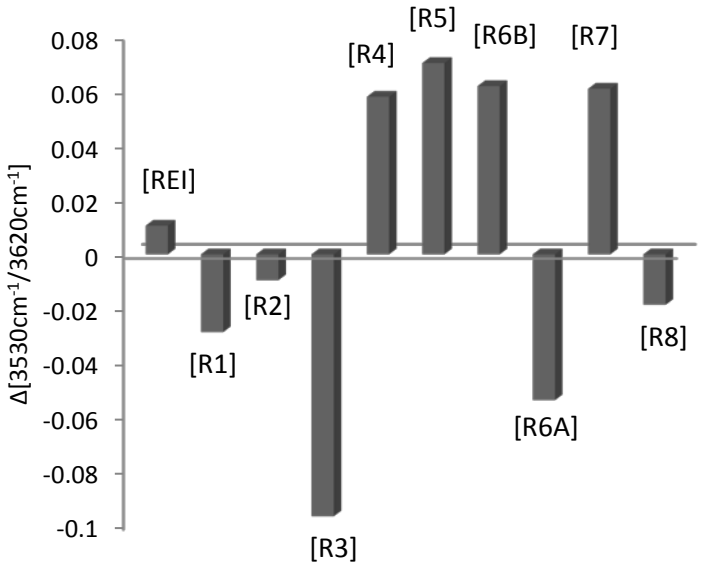

653

654 Figure 5

655

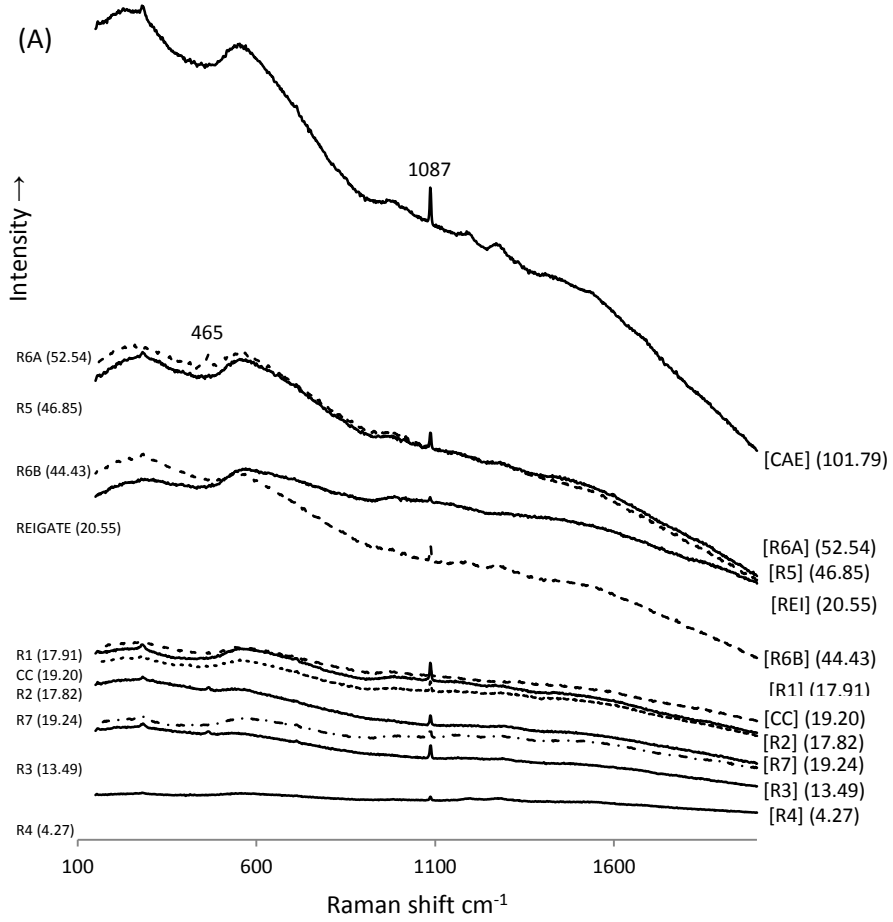

656

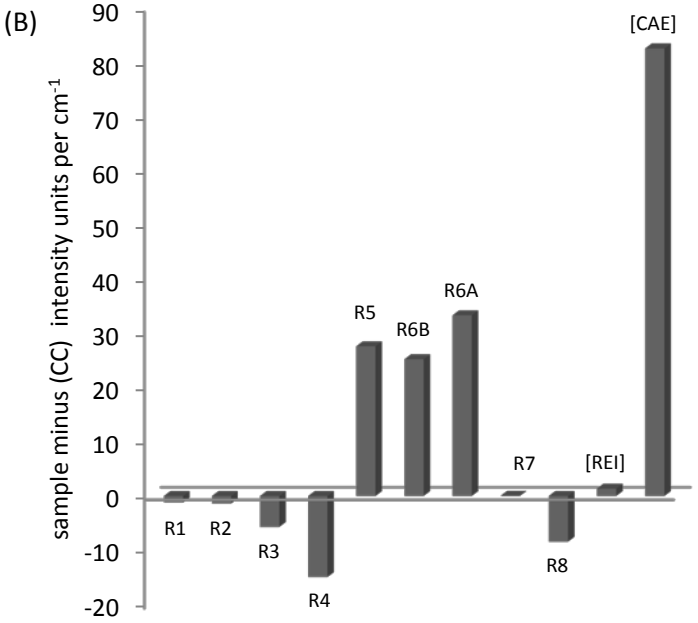

657

658 Figure 6

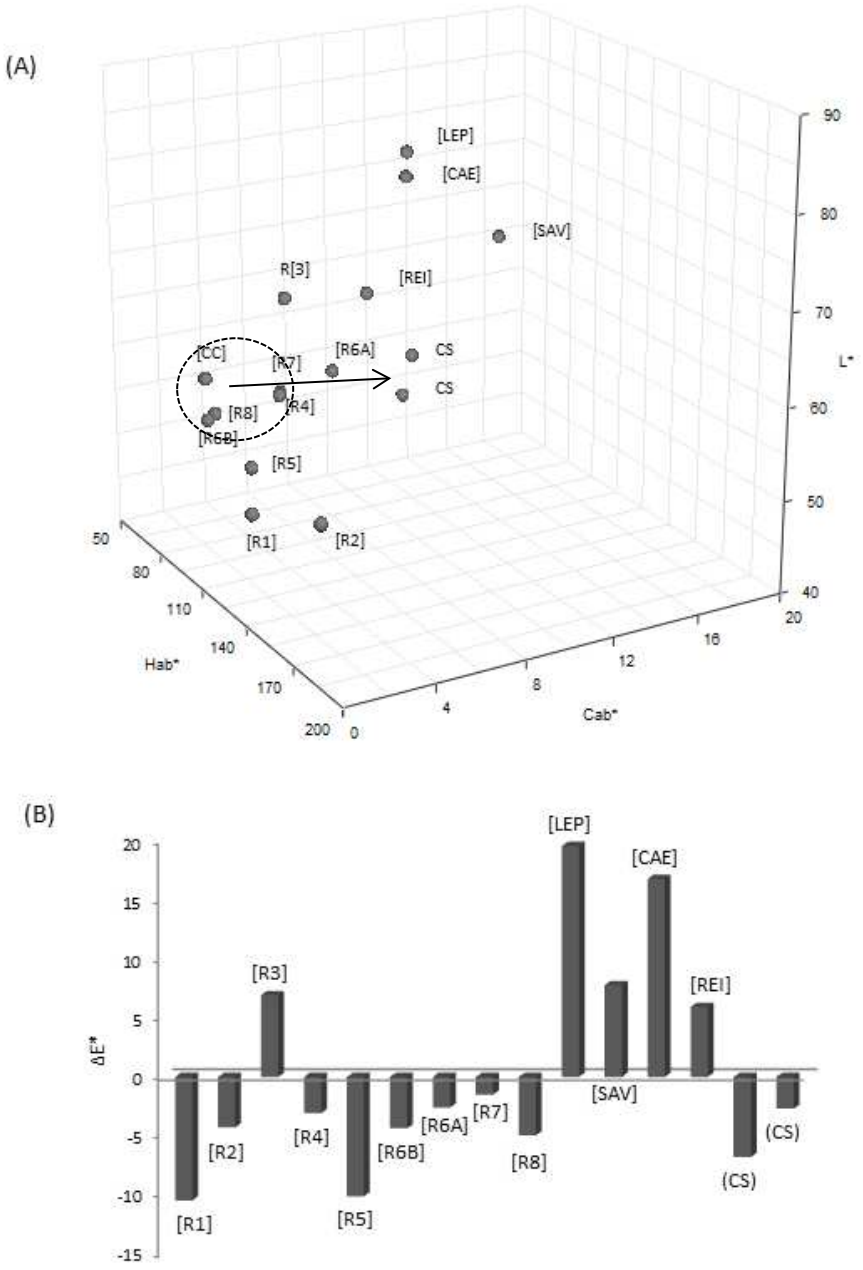

659

660 Figure 7